Optimization of Multi-Stage Hydraulic Fracturing in Unconventional Reservoirs in the Context of Stress Variations with Depth

Ankush Singh and Mark Zoback, Stanford University; Mark McClure, ResFrac Corporation

Abstract

Stage length and perforation cluster spacing are important design parameters for multi-stage hydraulic fracturing. This study aims to demonstrate that the interplay between subtle variations of the least principal stress (S_{hmin}) with depth and the stress shadows induced by simultaneously propagating hydraulic fractures from multiple perforation clusters, primarily determines the propped and fractured area in the target formations. This principle is illustrated with the help of a case study in a prolific unconventional formation in the north eastern US, where the vertical stress variations are well characterized through discrete multi-depth stress measurements and actual stage design parameters used by the operator are known. At first, we show how the hydraulic fracture footprint and proppant distribution varies with a change in the vertical stress profile. The stress profile is shown to be a very important in determining the optimal vertical and lateral well spacing. The evolution of the stress shadow in the different layers is shown during the pumping as the fracture propagates across multiple layer boundaries. Subsequently, we demonstrate that by changing the magnitude of stress perturbations caused by the stress shadow effect, the distribution of propped area can be altered significantly. We use this method to determine the optimal cluster spacing keeping other design parameters constant such as flow rate, perforation diameter, etc. Simulations from selected cluster spacing realizations are run with high and low permeability scenarios to show the importance of correct matrix permeability inputs in determining the three-dimensional depletion profile and ultimate production. By varying the cluster spacing we show the hydraulic fracture propagation change from being solely stress layering driven to stress shadow influenced. The effect of stress shadow on the final fracture footprint is highly specific depending on the given stress layering and is thus case-dependent. This study demonstrates that knowledge of stress variations with depth and modeling are critical for optimizing stimulation efficiency.

Introduction

Stage length and perforation cluster spacing are important design parameters for multi-stage hydraulic fracturing in unconventional reservoirs. This study builds on the work done by Singh et al. (2019) and aims to demonstrate that the interplay between least principal stress (S_{hmin}) variations with depth and the stress

shadows induced by simultaneously propagating hydraulic fractures from multiple perforation clusters primarily determines propped area in the target formations.

Vertical variations of least principal stress (S_{hmin}) are well known to control vertical hydraulic fracture growth (e.g. Fisher & Warpinski, 2012; Xu & Zoback, 2015; Alalli & Zoback, 2018; Zoback & Kohli, 2019). In addition to the upward or downward fracture growth, stress layering can have a significant impact on proppant distribution, and cluster efficiency (Zhang & Dontsov, 2018; Singh et al., 2019). Despite the importance of characterizing variations of stress magnitude with depth, multi-depth stress measurements targeting layers within, above and below producing formations are often exceedingly rare.

Through modeling, Fu et al. (2019) approximated the effect of a systematic stress layering (or stress roughness) by assuming an anisotropic fracture toughness in their simulations (with toughness higher in the vertical direction). This implicit approach might be useful to account for low wavelength systematic stress variations, such as the effect of thin clay-rich layers characterized by unusually high values of high S_{hmin} as thin layers are also unlikely to act as strong stress barriers. However, the longer wavelength stress variations need to be explicitly modeled to evaluate whether they have a significant impact on hydraulic fracture growth. These would include stress changes across known lithological boundaries. Xu & Zoback (2015) and Ma & Zoback (2017) demonstrate cases studies in two unconventional plays, where the larger scale vertical variations in S_{hmin} were determined from Diagnostic Fracture Injection Tests (DFITs) performed at multiple stratigraphic intervals either in the same well or nearby offset wells. These measurements are consistent with fracture dimensions estimated from the spatial distribution of microseismic events (Xu & Zoback, 2015).

The stress changes in the vicinity of an open propagating hydraulic fracture are referred to as the stress shadow. These stress changes occur due to the mechanical compression of the matrix perpendicular to the fracture face which leads to an increase in S_{hmin} (Warpinski & Branagan, 1989; Fisher et al., 2004; Warpinski et al., 2013). The stress shadow also leads to a decrease in S_{hmin} ahead of the fracture tip (Soliman et al., 2008; Warpinski et al., 2013; Daneshy, 2014; Barthwal & van der Baan, 2019; Kettlety et al., 2020). Direct strain rate observations from Digital Acoustic Sensing (DAS) monitoring in offset wells have also confirmed the presence of significant stress shadow effect in hydraulic fracturing operations (Jin & Roy, 2017). In addition to the mechanical opening, fluid leak-off from a hydraulic fracture into the surrounding matrix can lead to an increase in S_{hmin} from poroelastic effects (Detournay et al., 1989; Vermylen & Zoback, 2011; Salimzadeh et al., 2017). The stress shadow effect has a major impact on fractures propagating in close proximity (Roussel & Sharma, 2011; Agarwal et al., 2012; Warpinski et al., 2013).

For a specified injection scheme, a single hydraulic fracture will have a footprint governed primarily by the stress layering. As fractures start to propagate in close proximity to each other, however, the stress shadow will start playing a role in modifying the fracture footprint. The exact fracture footprint resulting from a stimulation is a complex function of the relative impact of two effects in three dimensions. We illustrate this by modeling a real case study in a prolific unconventional play in the north eastern US. The S_{hmin} variations with depth are characterized through five DFITs conducted in a vertical pilot well. The DFITs were conducted to measure S_{hmin} variations in lithological layers above, below and in the intended landing zone for horizontal producers. The measurements show that the in-situ stress configuration is unfavorable for optimal stimulation of the target zones. This is combined with the actual stimulation parameters and detailed reservoir characterization from a nearby offset well to model the hydraulic fracture growth and subsequent gas production with varying stage length and cluster spacing. We compare the simulation results with an idealized stress configuration where the landing zone is surrounded above and below by prominent stress barriers, using the same input operational realizations. The simulations were performed using ResFrac (McClure & Kang, 2017; McClure & Kang, 2018), a 3-D fully integrated fluid flow and hydraulic fracture propagation code.

In the sections that follow, we focus our investigations to address the following questions:

1. How does the propped area of hydraulic fractures vary with changes in the vertical stress layering in the absence of stress perturbations from nearby fractures?
2. How does the stress shadow evolve during pumping in the different stress layers?
3. Does changing the stress shadow by adjusting the cluster spacing change the propped and fractured area in the target zones in a systematic fashion for a given stress profile?
4. How does a change in permeability affect the optimal cluster spacing decision for a given stress profile and stress shadow configuration?

Simulation Methodology

Fluid flow in the matrix is modeled with a finite volume method. Fluid flow from the fractures to the matrix and vice-versa is modeled using a 1D subgrid method developed by McClure (2017). Fracture propagation is modelled using principles of linear elastic fracture mechanics with the assumption that fractures are planes that propagate parallel to the maximum horizontal stress (S_{Hmax}) without any bending. The observations of closely spaced hydraulic fractures with consistent orientations parallel to S_{Hmax} from recent drill-through studies support this assumption (Raterman et al., 2017; Gale et al., 2018). The fracture propagates when the stress intensity fracture exceeds the fracture toughness. A scale dependent fracture toughness model is used to control the fracture size using the following relations after Delaney et al. (1986) and Scholz (2010):

$$K_{IC} = K_{IC,init}\left(1 + \alpha\sqrt{L_{eff}}\right) \qquad 1$$

where K_{IC}, $K_{IC,init}$ are the initial and scaled fracture toughness values, while L_{eff} is the larger fracture dimension. The coefficient α multiplied with the fracture dimension term can be used as a tuning parameter if microseismic event distribution or other constraints for fracture geometry are available. For the present study, it is assumed to be 0.8. The fractures are assumed to retain conductivity and aperture after closure. The closed fracture aperture is computed as a function of the effective normal stress acting on the plane by the Barton-Brandis equation (Barton et al., 1985). Proppant transport is modelled taking into account properties including proppant grain size, proppant density, fluid viscosity, non-Newtonian rheology, and effects including gravitational convection, hindered settling, clustered settling and the effect of proppant on slurry viscosity (McClure & Kang, 2018). Proppant trapping due to fracture roughness or natural fracture intersections has not been included in the current study.

The stress shadow effect is modeled by computing the stress changes in the matrix surrounding the hydraulic fractures from:

a. Elastic response to the mechanical fracture opening
b. Poroelastic stress changes resulting from the pressure change in the matrix caused by fluid leak-off from the fracture.

The stress perturbations due to the mechanical opening are modeled using the higher order displacement discontinuity method of Shou et al. (1997). McClure & Kang (2018) demonstrated that the implementation reduces to the analytical solution of Sneddon (1946) for a constant pressure injection into a pre-existing fracture in an impermeable medium. The poroelastic stress changes are modeled using the thermoelsatic function developed by Nowacki (1986). A similar approach is also described by Wang (2001). The implementation is validated by McClure & Kang (2018) by matching the analytical solution for a constant pressure change by Nowacki (1986). The Biot coefficient is assumed to be 0.5 for all the simulations. Poroelastic stress changes can also influence subsequent stages in hydraulic fracturing operations (Vermylen & Zoback, 2011). The stress perturbation from previous stages are not taken into account in the study.

Geological and Geomechanical model: Input Simulation Parameters

Input data
The modeling inputs are based on an actual case study from a prolific unconventional formation in the NE US. The case study consists of two wells referred to as ACS-1 and ACS-2, located about 18 miles apart. Both the wells target the same producing intervals with similar properties varying significantly only in depth and thickness. The overall setup of the model is similar to Singh et al. (2019) and Xu et al. (2019). The layer cake model consists of 6 layers A through F with layer D being the operator's primary target and layers E & F, the secondary targets.

Stress profile based on vertical well DFITs
The stress profile in the area is characterized by multi-depth diagnostic fracture injection test (DFIT) measurements conducted in ACS-1. Stress measurements were performed for all six lithological layers. Figure 1 shows the stress measurements along with the well log for the reservoir section. The computation of S_{hmin} from the DFITs was done by Xu et al. (2019). The DFIT measurements demonstrate a prominent vertical layering of the least principal stress across lithological boundaries. Xu et al. (2019) also showed that the stress layering can be explained by varying degrees of visco-elastic stress relaxation in the different lithological layers. Since, this area is known to be in a strike slip faulting regime, i.e. $S_{hmin}<S_v<S_{Hmax}$, formations with higher stress relaxation show an increased S_{hmin} as the stress state moves towards isotropic. Formations E and F show the highest degree of stress relaxation due to viscoelasticity and correspond to the low Gamma Ray part of the well log. Xu (2020) reports between 55-80% calcite in these formations from XRD data with the sample depths corresponding to the stress measurement depths in the respective formations.

   The stress profile determined from ACS-1 is assumed to be applicable to ACS-2. The S_{hmin} gradients computed in ACS-1 are used as input to compute the S_{hmin} in equivalent formations in ACS-2. The stress profiles for both wells in shown in Figure 2. The S_{hmin} within each layer is assumed to increase with depth. In order to highlight the effect of the stress layering on the fracture footprint, the simulations from ACS-1 and ACS-2 are compared to a hypothetical well H-1 with an idealized stress profile consisting of a low S_{hmin} pay bounded above and below by stress barriers (Figure 2).
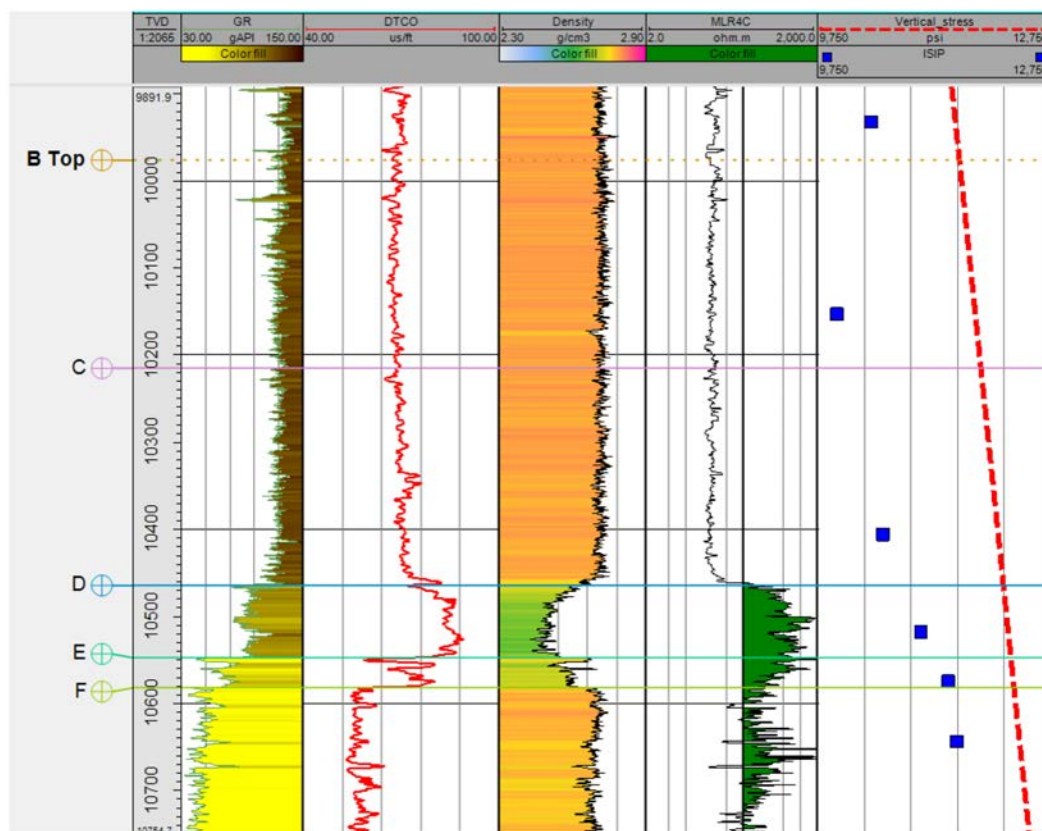
Figure 1—The stress measurements for the ACS-1 are shown by the instantaneous shut-in pressure (ISIP) values plotted as blue rectangles in the rightmost panel. The ISIP values indicate the magnitude of S_{hmin}. The red dashed line indicates the overburden stress. The measurements show a prominent lithology driven layering in S_{hmin} measurements. The logs shown from left to right are: gamma ray, compressional slowness, bulk density and formation resisvitiy.

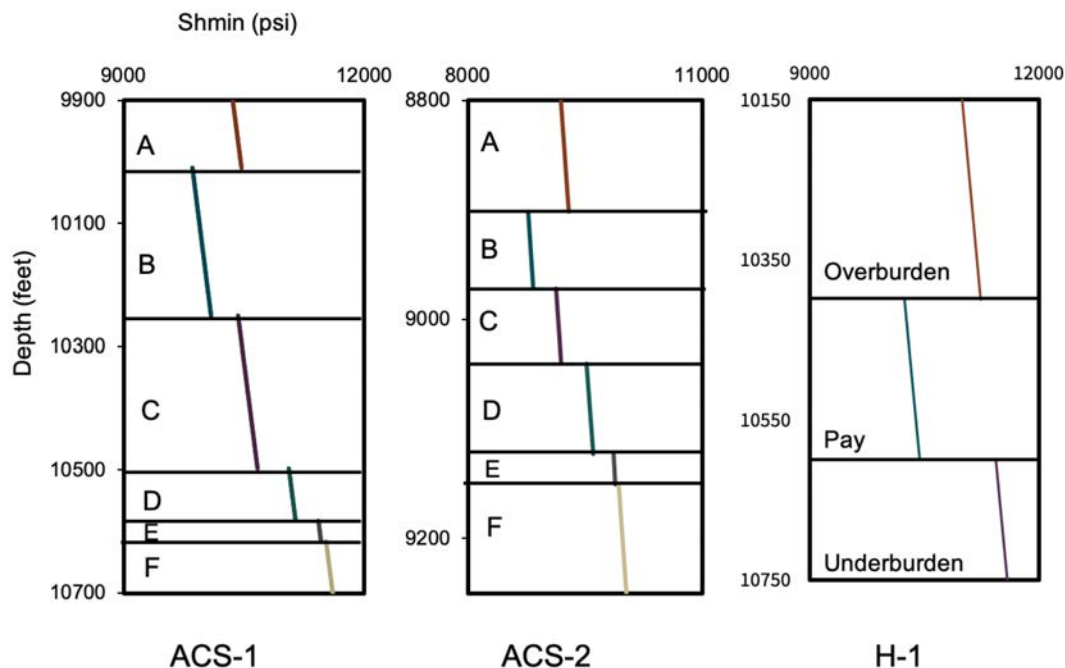Figure 2—S_{hmin} profiles with depth are shown for all the 3 cases. Stress profiles in ACS-1 and ACS-2 are based on DFIT measurements in the lithological layers in ACS-1. Stress magnitudes increase with depth within a formation and are offset at formation boundaries. H-1 has been assigned a hypothetical idealized stress profile that consists if a low S_{hmin} pay zone bounded by stress barriers above and below.

Reservoir characterization

The models use layer averaged properties determined from the well log and core-based characterization performed by the operator in ACS-2 (Table 1). The material properties derived from ACS-2 are assumed to be applicable to ACS-1. Layer D has the highest initial gas saturation and permeability making it the primary target zone. Layers E and F also have high initial gas saturation with a lower permeability making them the secondary targets. Layers B and C are tight and have a lower, but non-negligible gas saturation.

Table 1—Layer average properties determined from wells log and core analysis in ACS-2.

Formation	Top	Bottom	Porosity	Initial Gas Saturation (S_g)	Young's Modulus	Permeability
Name	*ft*	*ft*	*Porosity Units*	*fraction*	10^6 *psi*	*mD*
A	8148	8902	0.006	0.27	6.53	6.46e-05
B	8902	8970	0.02	0.69	5.6	2.3e-04
C	8970	9040	0.02	0.69	5.6	2.3e-04
D	9040	9123	0.06	0.94	4.37	1.4e-03
E	9123	9151	0.033	0.92	6.43	5.8e-04
F	9151	9296	0.01	0.8	9.17	1.2e-04

Operational Parameters

The actual field operational parameters from the stimulation of ACS-2 are used in the simulation runs with multiple perforation clusters. For the single fracture cases, the maximum injection rate is restricted to 20 bbl/min to avoid unrealistic values of perforation friction pressure. Figure 3 shows the pumping schedule used in the multi-cluster simulations. Slick water is injected at a maximum rate of 88 bbl/min for ~2.5 hours. The proppant is injected in phases with the finer proppant first followed by the coarser proppant. The completion design includes a perforation diameter of 0.45" with 10 perforations per cluster. The viscosity of the fluid injected is a function of pressure and temperature. For the conditions modeled in the three cases, the viscosity varies between 1.5-3 cP. The fluid used in the model is an approximation of slickwater with a viscosity higher than pure water due to the addition of friction reducer solutes. The viscosity of the proppant-fluid mixture is also a function of proppant concentration and velocities within the respective grid cells.
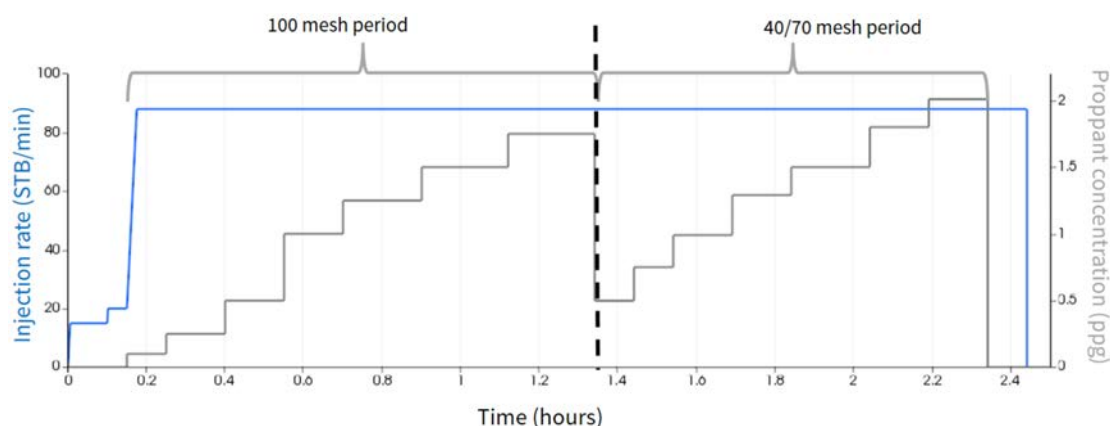
Figure 3—The operational parameters used for the multi-cluster simuations is shown, based on the actual stimulation design in ACS-2. The maximum injection rate is 88 bbl/min for about two and a half hours. 100 mesh and 40/70 mesh proppant are used with proppant concentration gradually increasing to a maximum value of 2 ppg.

Cases run

Table 2 shows a summary matrix of the cases modeled in the study. Single fracture simulations were performed for all three wells to demonstrate the fracture propagation purely driven by the stress layering. The second set of simulations involved plug-and-perf stages with three perforation clusters per stage and cluster spacing of 200 ft., 50 ft. and 20 ft. respectively. These simulations show the effect of increasing stress shadow by bringing the fractures closer over a wide range of cluster spacing. The propped fracture area and the total fracture area in the target formations are compared to see the change in stimulation efficiency as a function of decreasing cluster spacing and hence increasing stress shadows.

Table 2—A case map for the simulated cases is shown. The green shading corresponds to a well-simulation case pair that has been used in the analysis. The cases with five perforation clusters per stage are only analyzed for ACS-2 as they have a large computational time.

Cases	Well ACS-1	Well ACS-2	Well H-1
Single fracture case			
Three perforation clusters per stage: Stage length varying from 50-600 ft			
Three and five clusters per stage with realistic operational parameter space			
Permeability sensitivity			

Simulations modeling injection into three and five perforation clusters per stage simulations are performed in ACS-2 over a narrower stage length range, i.e. stage length varying from 60 ft. to 210 ft. at 30 ft. intervals. These correspond to varying the cluster spacing from 20 ft. to 70 ft. for the three cluster design and 12 ft. to 42 ft. for the five cluster design. These simulations demonstrate the application of the modeling into an operational decision-making process.

Selected simulations are repeated assuming a lower constant matrix permeability of 20 nD. The pressure depletion in the different layers from these simulations are compared to the reference permeability case to demonstrate the impact of permeability variations in deciding the optimal stimulation design.

Simulation Results and Discussion

Stress layering driven single fracture propagation
This section addresses how the hydraulic fracture footprint varies with changes in the vertical stress layering without the impact of stress perturbations from nearby fractures. The fracture propagation for a single isolated fracture is completely driven by stress layering. We simulated the propagation of a single fracture from an isolated perforation cluster placed in layer D for wells ACS-1, ACS-2 and in the central pay zone for well H-1. Figure 4 shows the resultant fracture footprint and aperture distribution for the three wells after the injection and month-long shut-in period. For ACS-1(Figure 4a), the fracture propagates upwards as the S_{hmin} in the overburden layers is significantly lower. The deeper, high S_{hmin} layers act as stress barriers to downward propagation. The higher thickness of the low stress layers causes the fracture to propagate a significant distance upwards till the upper stress barrier is encountered at the base of layer A. Consequently, this results in a high fracture height to width ratio and very low propped fracture area in layer D, which is the primary target layer. Similarly, for ACS-2 (Figure 4b) the fracture propagates upwards as well into layers B and C, and is restricted by the stress barrier at formation A. The smaller thickness of the low stress layers causes the fracture growth to have much lower height to width ratio. This would imply significantly different horizontal and vertical well spacings would be required for an efficient pad-scale development in the two cases. For H-1 (Figure 4c), the stress barriers at the top and bottom completely restrict the fracture growth in the pay zone. The aperture distribution is completely driven by the proppant placement, since the leak-off into the matrix over the shut-in period leads to closure of the unpropped parts of the fracture. The proppant settles down completely for ACS-2 and H-1, whereas for ACS-1 the proppant seems to screen out in layer C. The proppant screen-out due to the stress layering for ACS-1 is described on greater detail by Singh et al. (2019). Zhang & Dontsov (2018) also show examples of proppant screen-out due to stress layering. In both ACS-1 and ACS-2 there is suboptimal proppant placement in the main target layer D as well as the secondary targets layers E and F. The fracture propagates upwards driven by stress layering. Most of the energy from the injection is spent in stimulating layers B and C, which is not desirable. In contrast, for H-1 all of the fracture growth is confined to the intended zone and the stress layering aids in creating an optimal stimulation.
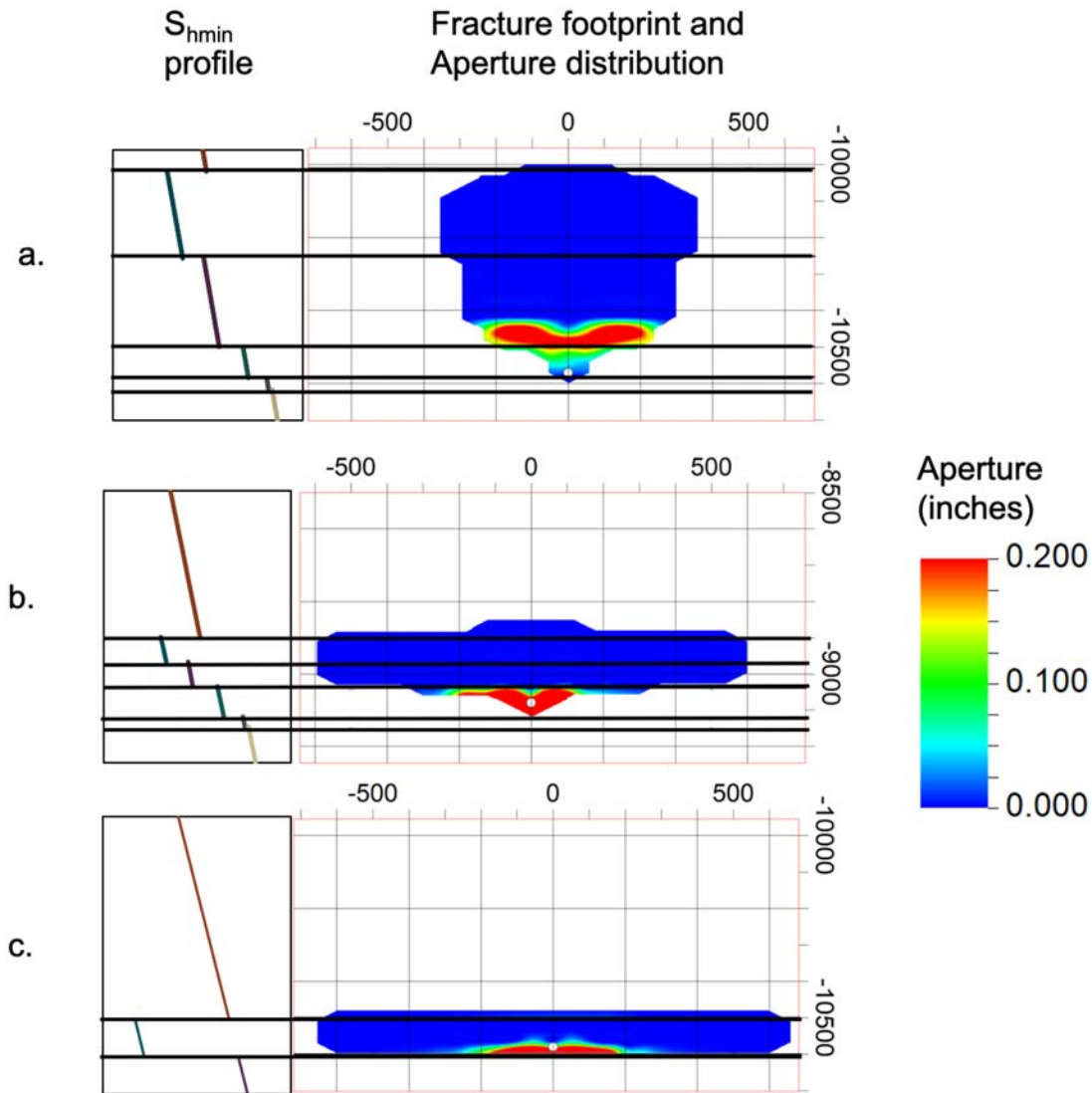
Figure 4—Hydraulic fracture propagation and aperture distribution for the single fracture case is shown for the three wells ACS-1, ACS-2 and H-1. The aperture distribution within the fracture is dominated by the proppant distribution with the red color showing regions of high final proppant concentration. The left panel shows the S_{hmin} profile with depth for all the three cases.

Stress shadow from a single fracture in 3D

In this section we use the example of ACS-1 single fracture case to address how the stress shadow in the different stress layers evolves during pumping. Figure 5 shows the fracture growth and aperture distribution five minutes, one hour and two hours into the pumping for ACS-1. Figure 6 shows the stress shadow generated by the injection in ACS-1 over the course of the pumping along depth slices S1-S1', S2-S2', S3-S3' in layers B, C and D. The depth slices are indicated in Figure 5 by the orange dashed lines. Initially the fracture starts in layer D and after 5 minutes of pumping, an increase in S_{hmin} is observed on the two sides of the fracture, while layer C sees a slight decrease in S_{hmin} due to tension ahead of the fracture tip. Layer B does not experience any stress shadow in the early stages of pumping. About an hour into the pumping, the fracture propagation is mainly taking place in layer C, which is evident from the high magnitude of compression on both sides of the fracture trace. Layers D and B experience decrease in S_{hmin} away from fracture center due to the tension caused by the tip of the propagating fracture in layer C. After two hours of injection, the fracture is propagating in layer B as seen by the stress shadow distribution, the stress shadow in layers C and D are more diffused at this point. These stress perturbations will have a significant impact

on the simultaneous growth of a nearby fractures as would be expected in a multi-cluster plug-and-perf hydraulic fracturing stage.
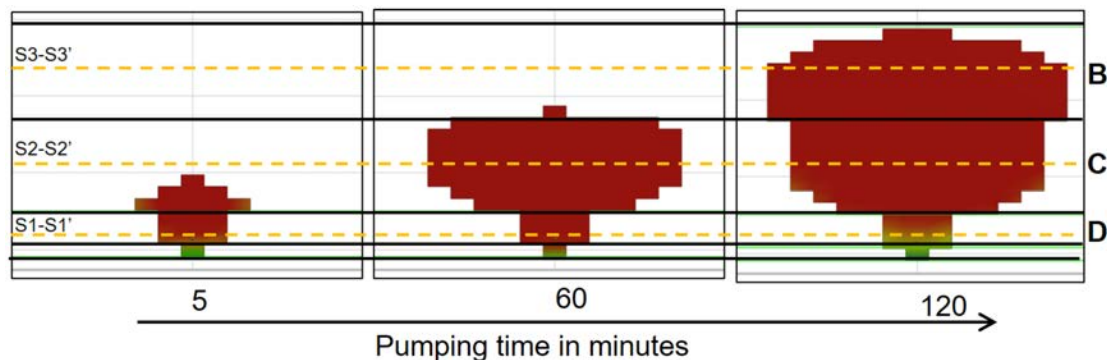

Figure 5—Snapshots of the fracture footprint and aperture distribution are shown at time intervals of five minutes, one hour and two hours into the injection. The fracture propagates upwards driven by the stress layering and the lower stress intervals have a wider aperture. The color indicates the open fracture aperture with the red being high aperture. The orange dashed lines indicate the position of the depth slices for Figure 6.
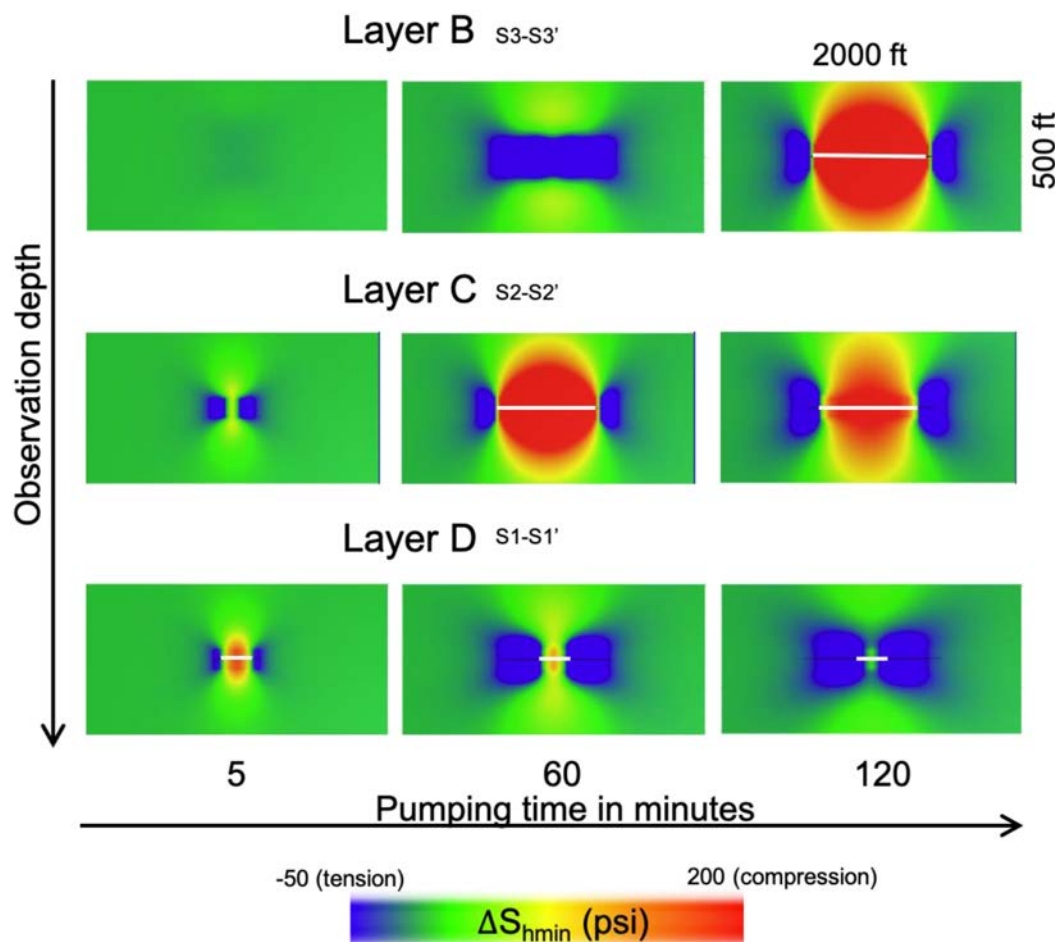

Figure 6—Perturbations in stress magnitudes parallel to the least principal stress direction are shown. The red color indicates increase in stress magnitude due to compression caused by mechanical opening and poroelastic effects. The blue color indicates a decrease in stress magnitude ahead of the fracture tip. The intersection of the fracture trace with the depth slice is indicated by the thick white lines. The positions of the depth slices are shown in Figure 5 by the orange dashed lines.

Effect on increasing stress shadow on a stage with multiple perforation clusters

In this section, we address whether changing the stress shadow by adjusting the cluster spacing changes the propped and fractured area in the target zones in a systematic fashion for a given stress profile. This variation in propped and fractured area can be used as a metric to decide the optimal cluster spacing.

As expected, the simulations with multiple perforation clusters per stage reveal significant variations in the fracture footprint and the eventual proppant placement compared to single isolated fractures. Figure 7 shows an example of fractures propagating from a 150 ft. stage with three clusters in ACS-2. The fracture configuration is severely affected by stress shadows and we observe significant proppant placement and fracture propagation in layers D, E and F in the central fracture, which experiences stress perturbations from both sides. In contrast, the single fracture case showed entirely upward propagation (Figure 4). The magnitude of the stress shadow increases with the closer spacing of perforation clusters and higher fluid injected per cluster. This causes a change in the vertical distribution of propped and total fracture area in the different layers. We hypothesize that we can utilize this variation to find the cluster spacing that maximizes the propped area in the primary and secondary target layers.
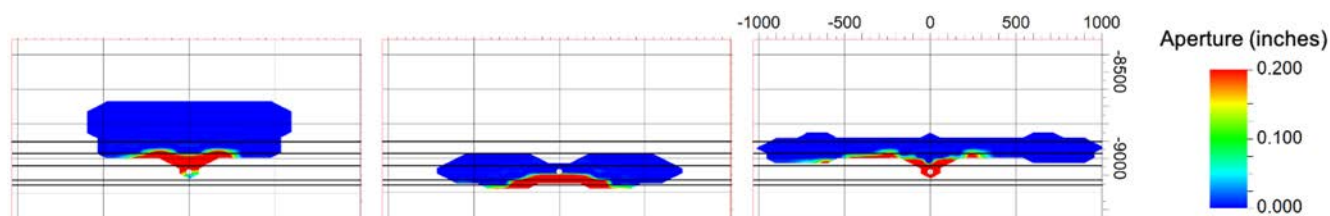

Figure 7—Final hydraulic fracture footprint and aperture distribution with injection in a 150 ft. stage in ACS-2. The tight cluster spacing of 50 ft. causes the fractures to experience the stress perturbations from neighboring fractures. The stress shadow causes fracture gorwth into zones that would remain unstimulated if fracture growth is driven only by the in-situ stress layering. This leads to significant propped area the bottom layers.

To test the sensitivity of propped area with change in stress shadow, we modeled injection into a plug-and-perf stage with three and five perforation clusters, with stage length from varying from 60 ft. to 210 ft. in 30 ft. increments. This corresponds to varying cluster spacing between 20-70 ft. for the 3 cluster realizations and 12-42 ft. for the 5 cluster realizations. The range of stage length and cluster spacing considered in these simulations are consistent with the parameter space commonly considered by operators in the area.

The 3-cluster design has more fluid injected into individual clusters leading to larger fractures, whereas the 5 cluster designs fits the fractures more tightly causing an overall increase in stress shadow within the stage. Figure 8 shows the computed propped area for all the realizations. The total propped area in general decreases with increase in cluster spacing. The total propped area decreases in formation D with higher cluster spacing for the 3 cluster design, while remaining nearly constant in the 5 cluster case. Similarly, for formations D, E, F combined, the propped area decreases with an increase in cluster spacing for the 3 cluster design. There is no clear trend in the 5 cluster design with the 12 ft. cluster spacing showing considerably higher downward growth. The recommendation in this case would be to perform a stimulation with either a 90 ft. stage with 3 perforation clusters (30 ft. cluster spacing) or a 210 ft. stage with 5 perforation clusters (42 ft. cluster spacing). While the total amount of fluid and proppant injected is same in all cases, the 90 ft. stage with three perforation clusters maximizes the total propped area in the primary target layer.
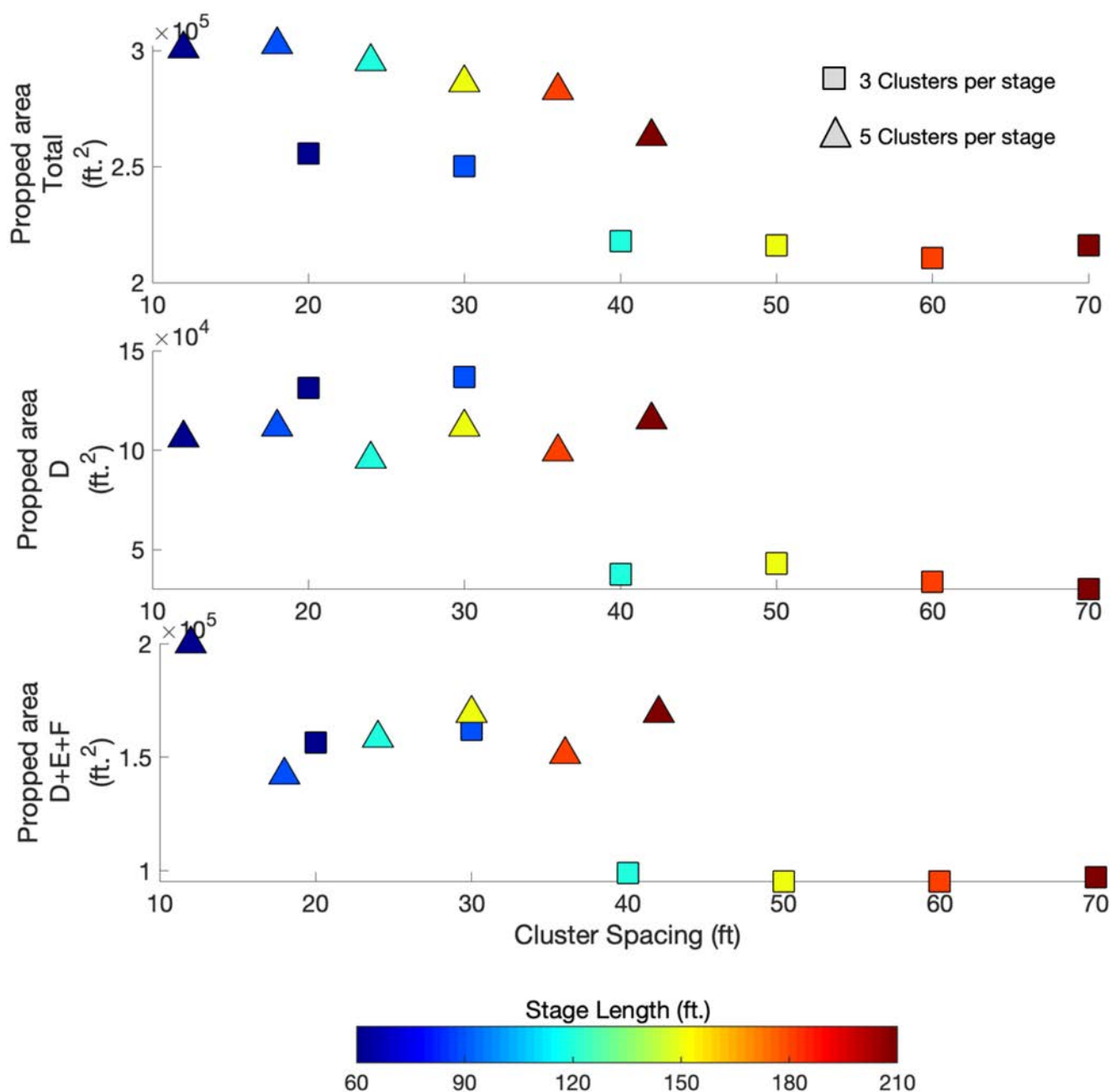
Figure 8—Propped area created as a function of varying cluster spacing is shown for the 3 and 5 cluster designs. The top row shows the total propped area, the middle row shows the propped area created in Layer D and the bottom row shows the propped area created in Layers D, E and F combined. The total propped area decreases with increae in cluster spacing for both the cases. For the 3 cluster case, the propped area in Layer D as well layers D, E and F combined decreases with an increase in cluster spacing with the 30 ft. spacing realization showing the best performance. For the 5 cluster, no significant change is noticed in the propped area created in layer D, with the 42 ft. cluster spacing showing the highest propped area. In the 5 cluster case, the 12 ft. cluster sapcing shows very high downward growth into layers E and F.

Figure 9 shows the total fractured area in all the cases. In the 5 cluster design, both the 42 ft. cluster spacing and the 12 ft. cluster spacing optimize the fracture surface area in formation D as well as formation D, E and F combined. For the 3 cluster cases, the total fracture area decreases with increase in cluster spacing beyond 30 ft. Therefore a 90 ft. stage with 3 perforation clusters or a 210 ft. stage with 5 perforation clusters optimize both propped and total fracture area. The total fracture area is also an important parameter as the unpropped fractures retain some conductivity after closure. While the contribution from shear stimulated natural fractures is not included in the model, it is quite obvious that increasing the total fracture surface

area would be beneficial in geological conditions where the contribution of the natural fracture network to fluid flow is significant.
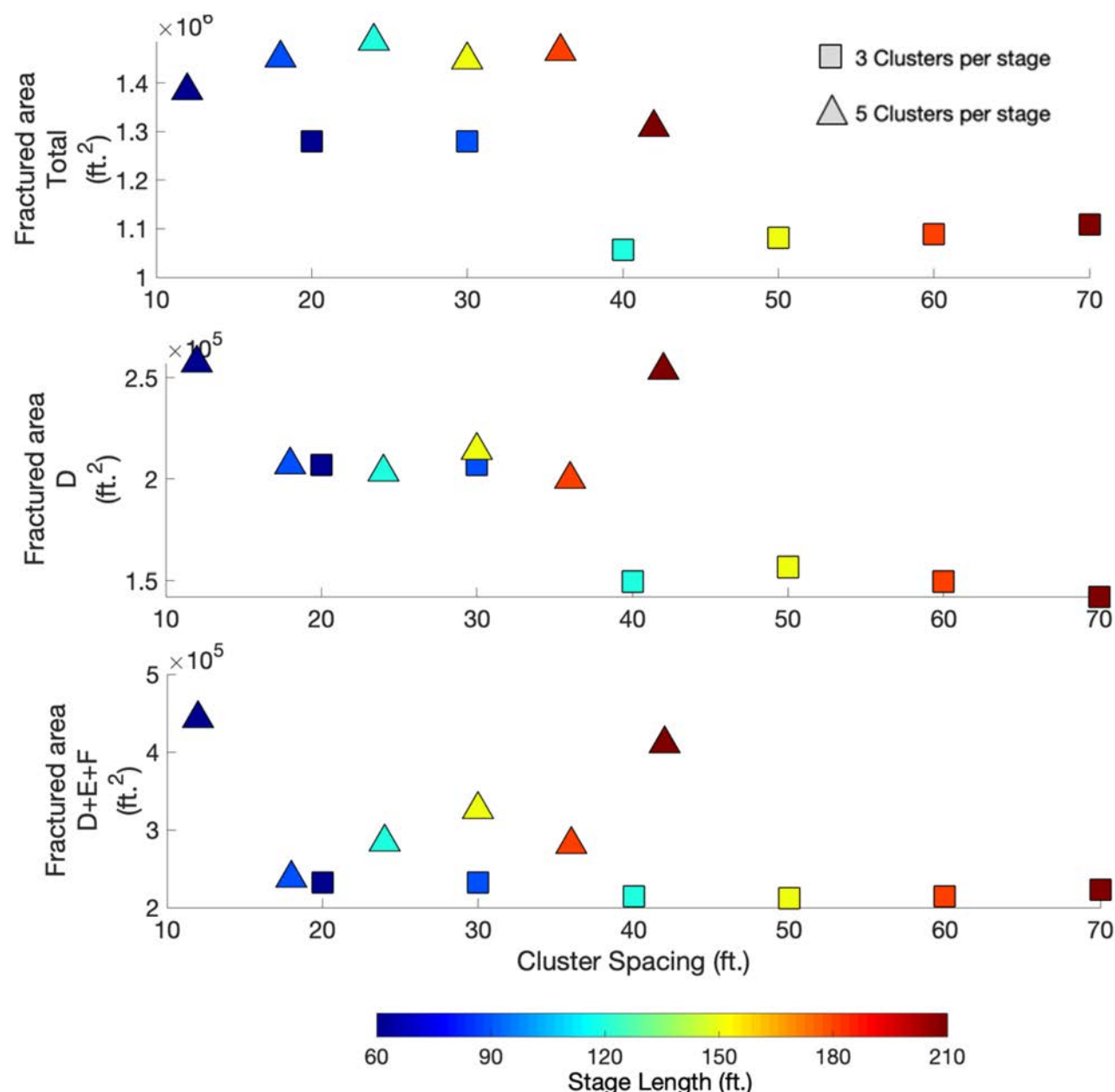

Figure 9—Fracture area created as a function of varying cluster spacing is shown for the 3 and 5 cluster designs. The top row shows the total propped area, the middle row shows the propped area created in Layer D and the bottom row shows the propped area created in Layers D, E and F combined. The total propped area decreases with increase in cluster spacing for the 3 cluster case, while it does not show any clear trend for the 5 cluster case. For the 3 cluster case, a cluster spacing of 30 ft. maximizes the fracture area in layer D, while for the 5 cluster case both the 12 ft. cluster spacing and the 42 ft. cluster seem to perform better than the other realizations.

For the cases with 5 clusters per stage, we investigated a wider parameter space to confirm if the propped area decreases with increase in cluster spacing. The results are described in detail in appendix A2 and show a consistent decrease in propped area in the target zones with an increase in cluster spacing.

Cumulative production per stage
Figure 10 and Figure 11 show the cumulative gas production per ft. of lateral length from the modeled stages with three and five clusters per stage. Production per ft. can be used as a proxy for recovery factor. In general,

the production per ft. of lateral length is expected to be higher for the tighter cluster spacing as there is lesser in-place volume targeted per perforation cluster in the stage. In addition, there is a significant overprint of the stress shadow induced variations in propped area. For the 3 cluster case, the proppant placement efficiency in the target zones varies significantly between the different realizations with the rapid decrease in propped area for realizations with cluster spacing higher than 30 ft., which corresponds to a stage length of 90 ft. This is also seen in the corresponding large drop in production per ft. for the longer stage realizations (Figure 10). For the 5 cluster case, the overall variation is less than the three cluster case, which is consistent with lower variation in the propped area. Also, the variation in propped area in some cases causes higher production per ft. in the larger stages. For example, the 150 ft. stage length has a larger production per ft. than the 120 ft. stage length. Majority of the gas production comes from layer D in all cases. Of course, the economic benefit of the additional production vis-à-vis the cost of the additional stages along the lateral length will drive the decision-making. The variation of propped area and consequently the production per stage are essential inputs in this decision-making process. An ideal metric would be some measure of the net present value (NPV), however discussion of the economic implications of additional stages vs. added production is beyond the scope of the present study.
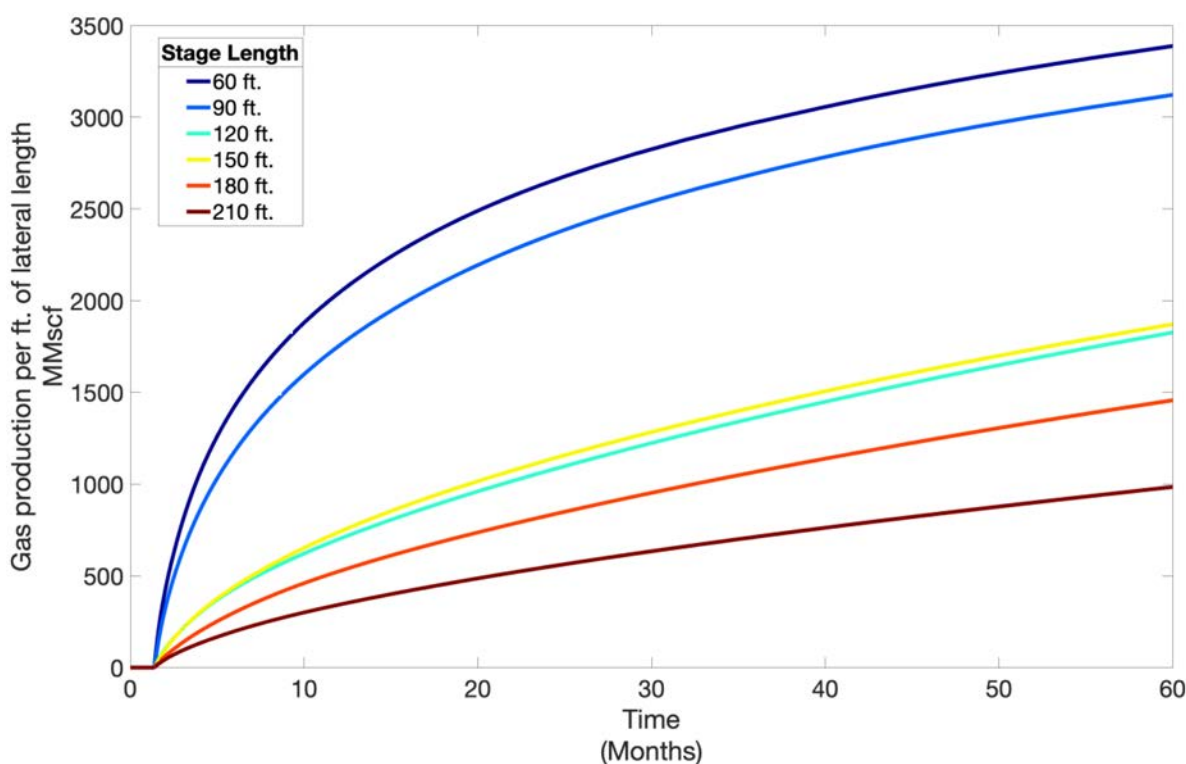

Figure 10—Cumulative gas production per foot of lateral length is shown for the all the realizations with three clusters per stage. The shorter stages as expected have greater production per foot and hence a better recovery factor. The large gap between the recovery factors of the 90 ft. stage and the longer stages is due to the significant variation in propped area.
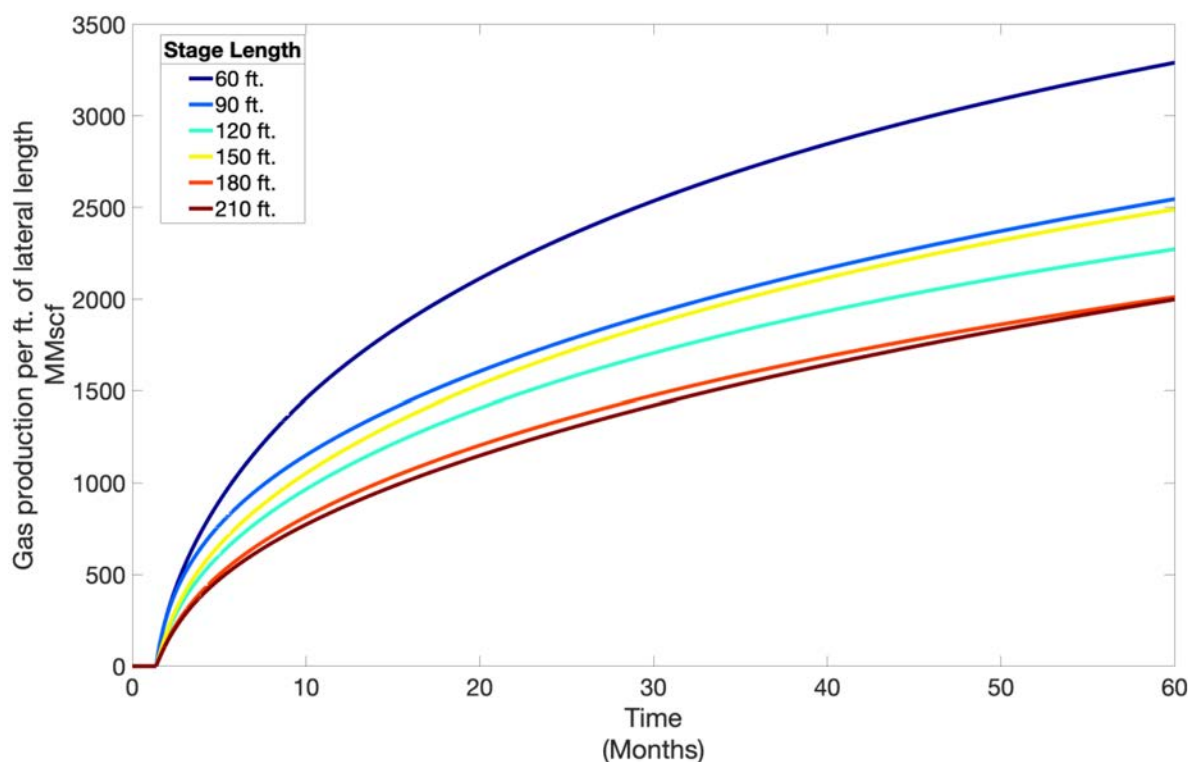
Figure 11—Cumulative gas production per foot of lateral length is shown for the realizations with five clusters per stage. The shorter stages, as expected have greater production per foot and hence a better recovery factor. The range in recovery factors is lower than the three cluster cases due to a lower variation in the propped area between the cases and the better performance of the longer stages in terms of the propped area.

Effect of permeability estimates

In this section, we address how a change in permeability affects the optimal cluster spacing decision for a given stress profile and stress shadow configuration. In addition to the propped area, the production also depends on unpropped fracture conductivity assumptions and most significantly the matrix permeability estimates. Figure 12 and Figure 13 show the pressure depletion in the recommended 3 cluster and 5 cluster stages using:

i.   Operator provided high layer wise permeability estimates
ii.   A constant lower permeability of 20 nD for all the layers, which is in agreement with recent published studies in the area.
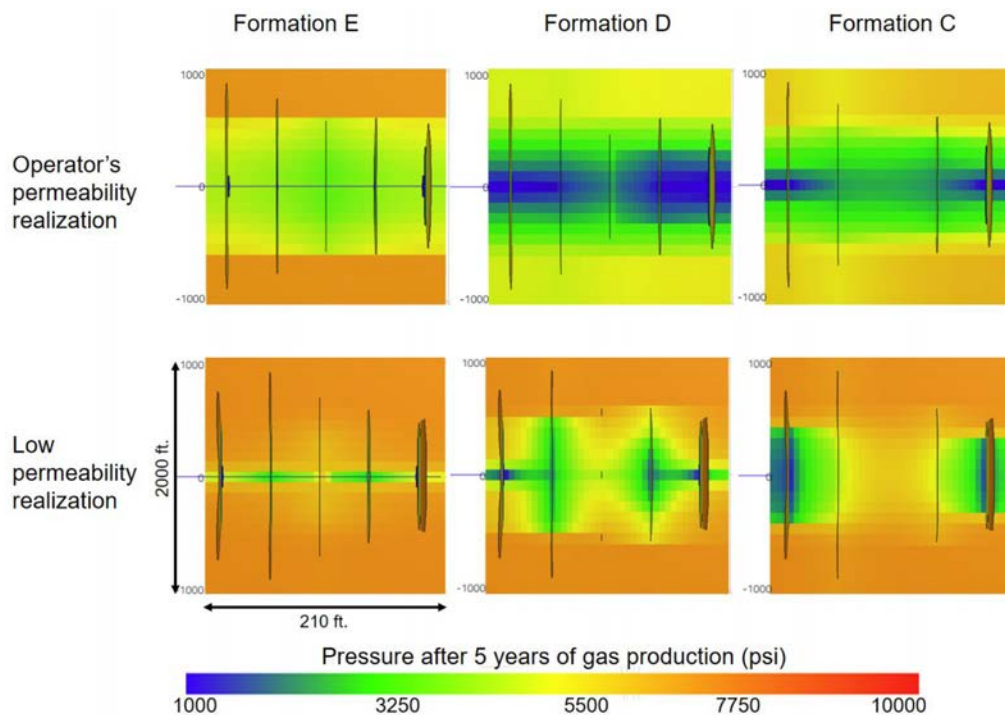
Figure 12—Variation in pressure depletion with permeability is shown for the 210 ft. stage with 5 clusters. With the operator's high permeability assumption, the fractures are able to drain most of the hydrocarbons in layer D. Significant depletion is also seen in layers E and C. With a lower permeability assumption, the depletion is confined to a small region besides the propped part of the fractures.

Figure 13—Variation in pressure depletion with permeability is shown for the 90 ft. stage with 3 clusters. With the operator's high permeability assumption, the fractures are able to drain most of the hydrocarbons in layer D. Significant depletion is also seen in layers E and C. With a lower permeability assumption, the depletion is confined to a small region besides the propped part of the fractures.
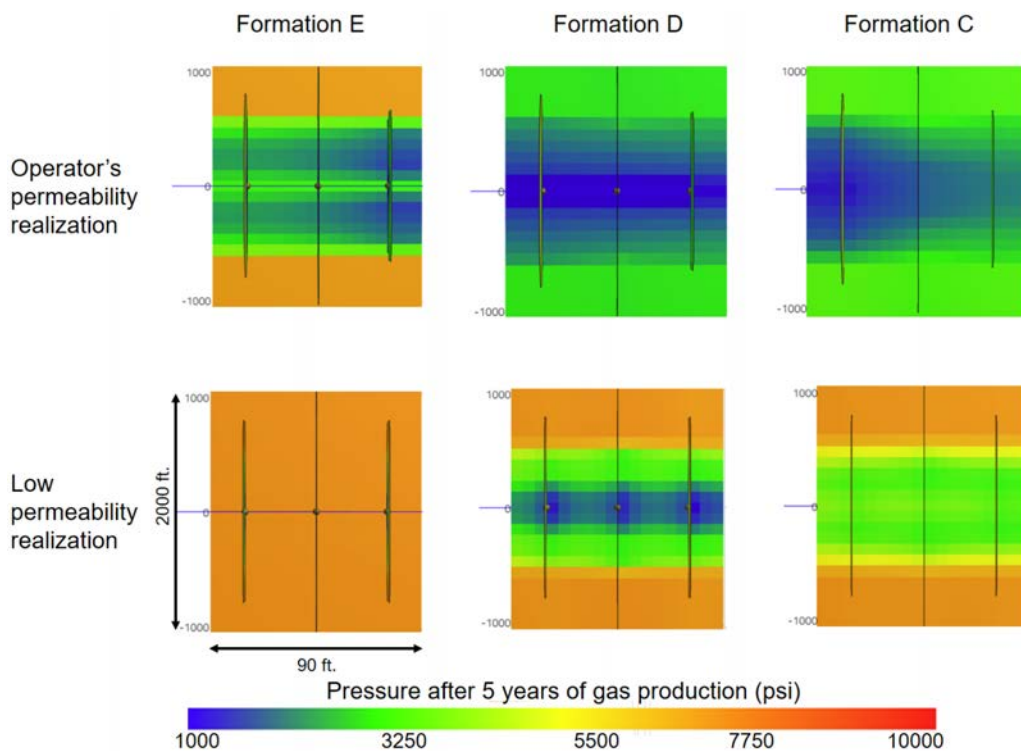
While permeability affects leak-off and in-turn the fracture propagation, the overall fracture footprint in these studies do not change significantly with change in permeability. In the higher permeability assumption, a single well propped fracture is able to drain most of the stage length effectively whereas in lower permeability assumption, the depletion from single fracture is constrained to a small distance from the fracture trace. In both the three and five cluster cases, layer D is well drained in the high permeability realization. Also, significant drainage is seen in the layers above and below. In the low permeability realizations, the layers above and below show only minor depletion. Also, layer D is fully depleted only up to a small distance from the fracture surface. In general, lower permeability should favor tighter cluster spacing. Fowler et al. (2019) demonstrated the effect of permeability estimates on history matching in a case study based in the Utica-Point Pleasant play.

Permeability determined from a history matching exercise has the problem of non-uniqueness as the production rate decline is proportional to the product of the propped area times the permeability (Fowler et al., 2019; Hakso & Zoback, 2019). A common workflow is to constrain the fracture area from the microseismic event locations and constrain permeability by performing rate transient analysis. However, we have demonstrated through the simulations that the total fracture area might not be a reasonable estimate of the propped area. Therefore, we recommend an independent estimate of permeability either from a post DFIT shut-in pressure decline analysis (McClure et al., 2019; Wang & Sharma, 2019) or core experiments (Heller et al., 2014) in addition to history matching of previous production data to calibrate permeability.

From solely stress layering driven to stress shadow influenced fracture propagation
We have demonstrated in the previous sections that increase in stress shadow has a major effect on the distribution of propped and fracture areas. Fracture propagation changes from entirely stress layering driven such as seen in the single fracture case to being increasingly influenced by stress shadow with tighter cluster spacing within a stage. To demonstrate this transition, we modeled injection into a stage with three perforation clusters and varied the cluster spacing over a wider range. The cluster spacing realizations considered were 200 ft., 50 ft. and 20 ft. The 200 ft. cluster spacing realization is clearly outside the parameter space considered in typical unconventional oil and gas development. These simulations were performed for all three wells.

Figure 14 shows the distribution of the fractured area and propped area with depth as a function of the cluster spacing over the wide range for ACS-2. From the distribution of stress shadows in Figure 6, it is clear that all of these realizations will have some influence of the stress shadow effect. The 200 ft. cluster spacing appears to be very similar to the single fracture case with almost no propped and fractured area in the layers D, E and F. An increase in the stress shadow influence by tightening the cluster spacing changes the fracture footprint significantly. There appears to significant downward fracture propagation in the 50 ft. and 20 ft. realizations. Unlike the single fracture case, all the realizations show upward propagation into layer A.
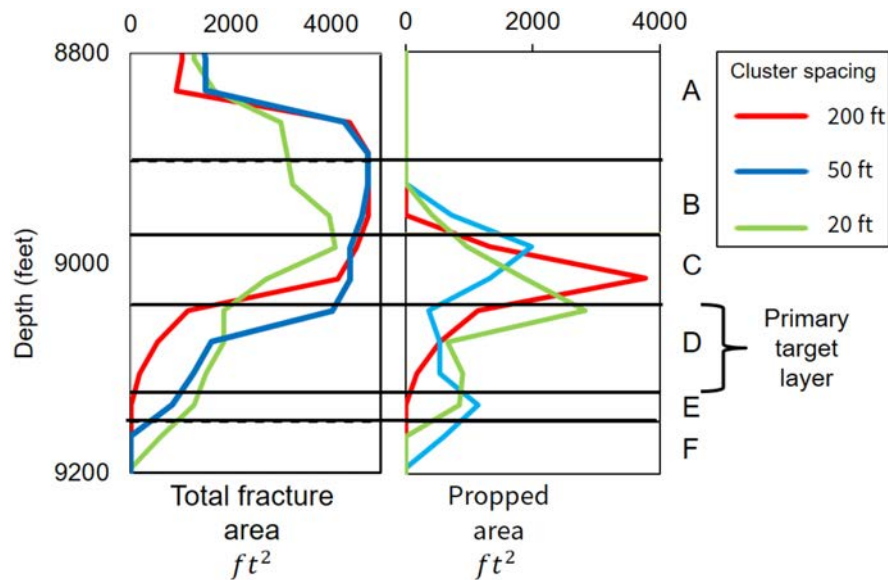
Figure 14—The distribution of total fracture and propped area with depth for well ACS-2 is shown for the 200 ft., 50 ft. and 20 ft. cluster spacing realizations. For the higher cluster spacing, there is relatively lower fracture area and propped area in the primary target layer D as well as the secondary target layers E and F.

While for ACS-2, increasing stress shadow causes a more optimal stimulation, the interaction between stress shadow and the stress layering is very complex and needs to be analyzed carefully for individual cases. For H-1, the stress layering is favorable for optimal stimulation of the pay zone. Figure 15 shows the distribution of propped and fracture area for H-1. The 200 ft. cluster spacing has the least stress shadow effect and hence, the highest fracture and propped area in the pay zone. Tighter cluster spacing increases the stress shadow causing out of zone fracture growth. In this case, the lowest stress shadow stage design should be optimal.
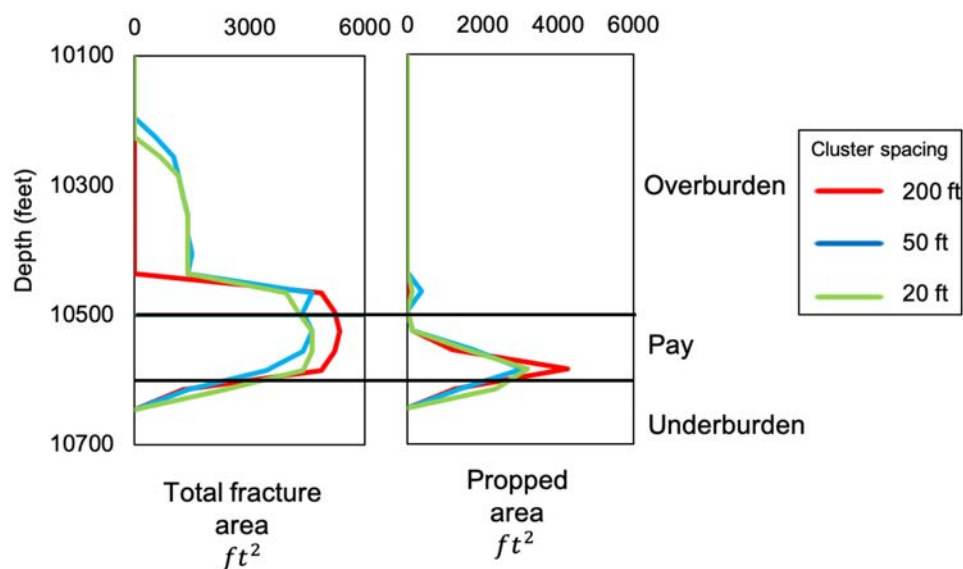
Figure 15—The distribution of total fracture area and propped area with depth for H-1 is shown for the 200 ft., 50 ft. and 20 ft. cluster spacing realizations. The 200 ft. realization maximizes the propped and total fracture area in the pay zone, while tighter cluster spacing increases upward and downward growth of the hydraulic fractures into the overburden and the underbruden.

This demonstrates that the effect of stress shadow on the final fracture footprint is highly variable depending on the stress layering configuration. Therefore, replication of an ideal cluster spacing across areas

with differing stress profiles might result in a suboptimal operational design. The fracture and propped area distributions for ACS-1 with varying cluster spacing are described in Appendix A2.

Conclusions

We investigated the complex 3-D interplay between the in-situ stress layering and the stress shadow effect through a series of simulations and demonstrated that combining knowledge of stress variations with depth and hydraulic fracture modeling is critical for optimizing stimulation efficiency. We analyzed the simulation results with respect to the following questions:

How does the propped area of hydraulic fractures vary with changes in the vertical stress layering in the absence of stress perturbations from nearby fractures?. The simulations demonstrate that the propagation of multiple hydraulic fractures in a stage is mainly governed by the in-situ stress layering with a significant influence of the stress shadow. Propagation of a single isolated perforation cluster per stage is an end member case completely driven by stress layering without any influence of the stress shadow effect. In the case studies for Wells ACS-1 & ACS-2, the unfavorable stress layering results in an upward fracture propagation with both the operator's primary and secondary targets having negligible fracture area and proppant placement. The variation of relative thicknesses of the high and low stress layers results in very different fracture aspect ratios in the two cases. Thus, determining the stress profile is essential in constraining vertical and horizontal well spacing for efficient pad scale developments. In the hypothetical, idealized well H-1 the single fracture case results in the desired stimulation and proppant placement in the pay zone.

How does the stress shadow evolve during pumping in the different stress layers?. We have demonstrated the three-dimensional stress shadow effect as function of time and observation depth for a given stress layering profile. As a fracture propagates across lithological boundaries, the distribution of the stress perturbation varies in the layers. In the well ACS-1, as the fracture propagates upwards into layers B and C, the stress perturbation increases in those layers, while remaining negligible in the target zone. The influence of the stress shadow extends to a significant distance (up to 200 ft. on each side) normal to the fracture when significant opening is observed in a particular stratigraphic layer. The reduction in S_{hmin} observed ahead of the fracture tip is consistent with analytical solutions and is observed both laterally ahead of the fracture tip and also in the layers above and below the current propagation layers.

Does changing the stress shadow by adjusting the cluster spacing change the propped and fractured area in the target zones in a systematic fashion for a given stress profile?. Simulations of injection into stages with multiple perforation clusters showed significant difference in fracture footprint and propped area distribution of the hydraulic fractures compared to the single fracture case. Significant downward fracture propagation was observed in ACS-2 in contrast with the single fracture case.

To test the sensitivity of propped area with change in stress shadow, we modeled injection into a plug-and-perf stage with three and five perforation clusters with stage length from varying from 60 ft. to 210 ft. in 30 ft. increments. This corresponds to varying cluster spacing between 20-70 ft. for the 3 cluster realizations and 12-42 ft. for the 5 cluster realizations. The sensitivity analysis revealed significant variation in propped area distribution between the layers with changes in cluster spacing. Overall, there was a clear general trend of decreasing propped area in the primary target layer with increase in cluster spacing with a few exceptions. We demonstrated how this workflow can be used to identify cluster spacing and stage length that maximizes both propped and overall fracture area in the target layers.

It is commonly known that the total fracture area is not a good estimate of the propped area in hydraulic fracturing operations. In addition, these simulations show that the optimal realizations might be different in some cases depending on whether total or propped fracture area is used as the optimizing metric. Even if the

microseismic event distribution is used to constrain the total fracture area, the history matching remains non-unique as the propped fracture area and the permeability both remain unknown. The propped fracture can only be estimated from production data if a reasonably accurate estimate of permeability is independently available.

Gas production per ft. of lateral length from all the stages was modeled as a function of the stage length and hence cluster spacing. Tighter cluster spacing is usually expected to have a higher production per ft. and hence a higher recovery factor as each cluster targets a lower in-place volume. Additionally, the general trend of increase in propped area in the target formations with a tighter cluster spacing leads to an even more significant increase in the recovery factors for the shorter stage in some cases. In some specific instances, the stress shadow induced propped area variations lead to a higher recovery factor for the longer stages.

The transition from a solely stress layering driven to stress shadow influenced fracture propagation is shown by modeling a wider range of cluster spacings. The simulations show that the effect of stress shadow on the propped area distribution is unique for a given stress profile. For example, while tighter cluster spacing leads to an increase in propped area in the target zone for ACS-2, H-1 shows the opposite trend. Thus, an accurate characterization of the vertical stress profile is essential in optimizing the stage design.

How does a change in permeability effect the optimal cluster spacing decision for a given stress profile and stress shadow configuration?.   In addition to the propped surface area, the decline in the production rates are dependent on the square root of the permeability. In addition to the operator provided high permeability realization, we ran the models with a lower permeability assumption in line with published studies from the area. In general, lower permeability favors tighter cluster spacing. The three-dimension depletion profile varies significantly with the different permeability assumptions. With the higher permeability assumptions, the propped fractures are able to drain hydrocarbons to a significant distance. Also, significant depletion is noticed in zones with unpropped fractures. In contrast, with a lower permeability assumption the depletion is restricted to a small distance near the fracture and much less depletion is noticed in the zones with unpropped fractures.

References

Agarwal, K., Mayerhofer, M. J., & Warpinski, N. R. (2012). Impact of geomechanics on microseismicity. In Society of Petroleum Engineers - SPE/EAGE European Unconventional Resources Conference and Exhibition 2012, 662–677. https://doi.org/10.2118/152835-ms

Alalli, A. A., & Zoback, M. D. (2018). Microseismic evidence for horizontal hydraulic fractures in the Marcellus Shale, southeastern West Virginia. *The Leading Edge*, **37**(5), 356–361. https://doi.org/10.1190/tle37050356.1

Barthwal, H., & van der Baan, M. (2019). Role of fracture opening in triggering microseismicity observed during hydraulic fracturing. *GEOPHYSICS*, **84**(3), KS105–KS118. https://doi.org/10.1190/geo2018-0425.1

Barton, N., Bandis, S., & Bakhtar, K. (1985). Strength, deformation and conductivity coupling of rock joints. *International Journal of Rock Mechanics and Mining Sciences & Geomechanics Abstracts*, **22**(3), 121–140. https://doi.org/10.1016/0148-9062(85)93227-9

Daneshy, A. A. (2014). Fracture Shadowing: Theory, Applications and Implications. In SPE Annual Technical Conference and Exhibition. https://doi.org/10.2118/170611-MS

Delaney, P. T., Pollard, D. D., Ziony, J. I., & McKee, E. H. (1986). Field relations between dikes and joints: Emplacement processes and paleostress analysis. *Journal of Geophysical Research*, **91**(B5), 4920. https://doi.org/10.1029/JB091iB05p04920

Detournay, E., Cheng, A. H. D., Roegiers, J. C., & McLennan, J. D. (1989). Poroelasticity considerations in In Situ stress determination by hydraulic fracturing. *International Journal of Rock Mechanics and Mining Sciences And*, **26**(6), 507–513. https://doi.org/10.1016/0148-9062(89)91428-9

Fisher, M. Kevin, & Warpinski, N. R. (2012). Hydraulic-Fracture-Height Growth: Real Data. *SPE Production & Operations*, **27**(01), 8–19. https://doi.org/10.2118/145949-PA

Fisher, M.K., Heinze, J. R., Harris, C. D., Davidson, B. M., Wright, C. A., & Dunn, K. P. (2004, April 4). Optimizing Horizontal Completion Techniques in the Barnett Shale Using Microseismic Fracture Mapping. SPE Annual Technical Conference and Exhibition. https://doi.org/10.2118/90051-MS

Fowler, G., McClure, M., & Cipolla, C. (2019). A Utica case study: The impact of permeability estimates on history matching, fracture length, and well spacing. Proceedings - SPE Annual Technical Conference and Exhibition, 2019-September. https://doi.org/10.2118/195980-ms

Fu, P., Huang, J., Settgast, R. R., Morris, J. P., & Ryerson, F. J. (2019). Apparent toughness anisotropy induced by "roughness" of in-situ stress: A mechanism that hinders vertical growth of hydraulic fractures and its simplified modeling. *SPE Journal*, **24**(5), 2148–2162. https://doi.org/10.2118/194359-PA

Gale, J. F. W., Elliott, S. J., & Laubach, S. E. (2018). Hydraulic Fractures in Core From Stimulated Reservoirs: Core Fracture Description of HFTS Slant Core, Midland Basin, West Texas. In Unconventional Resources Technology Conference, Houston, Texas, 23-25 July 2018 (pp. 1340-1357). https://doi.org/10.15530/urtec-2018-2902624

Hakso, A., & Zoback, M. (2019). The relation between stimulated shear fractures and production in the Barnett Shale: Implications for unconventional oil and gas reservoirs. *GEOPHYSICS*, **84**(6), B461–B469. https://doi.org/10.1190/geo2018-0545.1

Heller, R., Vermylen, J., & Zoback, M. (2014). Experimental investigation of matrix permeability of gas shales. *AAPG Bulletin*, **98**(5), 975–995. https://doi.org/10.1306/09231313023

Jin, G., & Roy, B. (2017). Hydraulic-fracture geometry characterization using low-frequency das signal. *Leading Edge*, **36**(12), 975–980. https://doi.org/10.1190/tle36120975.1

Kettlety, T., Verdon, J. P., Werner, M. J., & Kendall, J. M. (2020). Stress Transfer From Opening Hydraulic Fractures Controls the Distribution of Induced Seismicity. *Journal of Geophysical Research: Solid Earth*, **125**(1). https://doi.org/10.1029/2019JB018794

Ma, X., & Zoback, M. D. (2017). Lithology-controlled stress variations and pad-scale faults: A case study of hydraulic fracturing in the Woodford Shale, Oklahoma. *Geophysics*, **82**(6), ID35–ID44. https://doi.org/10.1190/geo2017-0044.1

McClure, M. (2017). *An accurate and efficient method for calculating fluid exchange between fractures and matrix with a non-conforming mesh*. arXiv preprint arXiv:1709.02493. http://arxiv.org/abs/1709.02493

McClure, M., Bammidi, V., Cipolla, C., Cramer, D., Martin, L., Savitski, A. A., Sobernheim, D., & Voller, K. (2019, July 25). A collaborative study on DFIT interpretation: Integrating modeling, field data, and analytical techniques. In Unconventional Resources Technology Conference, Denver, Colorado, 22-24 July 2019 (pp. 2020-2058). https://doi.org/10.15530/urtec-2019-123

McClure, M., & Kang, C. (2018). *ResFrac Technical Writeup*. arXiv preprint arXiv:1804.02092. http://arxiv.org/abs/1804.02092

Mcclure, M. W., & Kang, C. A. (2017). A Three-Dimensional Reservoir, Wellbore, and Hydraulic Fracturing Simulator that is Compositional and Thermal, Tracks Proppant and Water Solute Transport, Includes Non-Darcy and Non-Newtonian Flow, and Handles Fracture Closure SPE-182593. SPE Reservoir Simulation Conference in Montgomery, TX 20-22 February 2017. https://doi.org/10.1021/ol201758a

Nowacki, W. (1986). *Thermoelasticity*, 2nd edn. Pergamon Press.

Raterman, K. T., Farrell, H. E., Mora, O. S., Janssen, A. L., Busetti, S., McEwan, J., Roy, B., Friehauf, K., Rutherford, J., Rutherford, J., Reid, R., Jin, G., Roy, B., & Warren, M. (2017). Sampling a Stimulated Rock Volume: An Eagle Ford Example. In Unconventional Resources Technology Conference, Austin, Texas, 24-26 July 2017 (pp. 937-954). https://doi.org/10.15530/urtec-2017-2670034

Roussel, N. P., & Sharma, M. M. (2011). Optimizing fracture spacing and sequencing in horizontal-well fracturing. *SPE Production and Operations*, **26**(2), 173–184. https://doi.org/10.2118/127986-PA

Salimzadeh, S., Usui, T., Paluszny, A., & Zimmerman, R. W. (2017). Finite element simulations of interactions between multiple hydraulic fractures in a poroelastic rock. *International Journal of Rock Mechanics and Mining Sciences*, **99**, 9–20. https://doi.org/10.1016/j.ijrmms.2017.09.001

Scholz, C. H. (2010). A note on the scaling relations for opening mode fractures in rock. *Journal of Structural Geology*, **32**(10), 1485–1487. https://doi.org/10.1016/j.jsg.2010.09.007

Shou, K.-J., Siebrits, E., & Crouch, S. L. (1997). A higher order displacement discontinuity method for three-dimensional elastostatic problems. *International Journal of Rock Mechanics and Mining Sciences*, **34**(2), 317–322. https://doi.org/10.1016/S0148-9062(96)00052-6

Singh, A., Xu, S., Zoback, M., & McClure, M. (2019). Integrated Analysis of the Coupling Between Geomechanics and Operational Parameters to Optimize Hydraulic Fracture Propagation and Proppant Distribution. SPE Hydraulic Fracturing Technology Conference and Exhibition. https://doi.org/10.2118/194323-MS

Sneddon, I. N. (1946). The distribution of stress in the neighbourhood of a crack in an elastic solid. Proceedings of the Royal Society of London. Series A. Mathematical and Physical Sciences, **187**(1009), 229–260. https://doi.org/10.1098/rspa.1946.0077

Soliman, M. Y., East, L. E., & Adams, D. L. (2008). Geomechanics Aspects of Multiple Fracturing of Horizontal and Vertical Wells. *SPE Drilling & Completion*, **23**(03), 217–228. https://doi.org/10.2118/86992-PA

Vermylen, J. P., & Zoback, M. D. (2011). Hydraulic fracturing, microseismic magnitudes, and stress evolution in the Barnett Shale, Texas, USA. Society of Petroleum Engineers - SPE Hydraulic Fracturing Technology Conference 2011, 556–570. https://doi.org/10.2118/140507-ms

Wang, H. F. (2001). *Theory of Linear Poroelasticity with Applications to Geomechanics and Hydrogeology*. Princeton University Press. https://doi.org/10.1515/9781400885688

Wang, H. Y., & Sharma, M. M. (2019). A novel approach for estimating formation permeability and revisiting after-closure analysis of diagnostic fracture-injection tests. *SPE Journal*, **24**(4), 1809–1829. https://doi.org/10.2118/194344-PA

Warpinski, N. R., & Branagan, P. T. (1989). Altered-stress fracturing. *JPT, Journal of Petroleum Technology*, **41**(9), 990–997. https://doi.org/10.2118/17533-pa

Warpinski, N. R., Mayerhofer, M., Agarwal, K., & Du, J. (2013). Hydraulic-Fracture Geomechanics and Microseismic-Source Mechanisms. *SPE Journal*, **18**(04), 766–780. https://doi.org/10.2118/158935-PA

Xu, S., Singh, A., & Zoback, M. D. (2019). *Variation of the least principal stress with depth and its effect on vertical hydraulic fracture propagation during multi-stage hydraulic fracturing*. American Rock Mechanics Association.

Xu, S. (2020). *In situ stress prediction from ductile deformation of unconventional reservoir rocks and its relation to the stress dependence of permeability*. (Doctoral dissertation, Stanford University)

Xu, Shaochuan, & Zoback, M. D. (2015). Analysis of stress variations with depth in the Permian Basin Spraberry / Dean / Wolfcamp Shale. In 49th US Rock Mechanics/Geomechanics Symposium.

Zhang, F., & Dontsov, E. (2018). Modeling hydraulic fracture propagation and proppant transport in a two-layer formation with stress drop. *Engineering Fracture Mechanics*, **199**, 705–720. https://doi.org/10.1016/j.engfracmech.2018.07.008

Zoback, M. D., & Kohli, A. H. (2019). *Unconventional Reservoir Geomechanics*. Cambridge University Press. https://doi.org/10.1017/9781316091869

Appendix

Five perforation clusters stage design: Propped area as a function of cluster spacing for a wide range of input parameters

For the cases with 5 clusters per stage, we investigated a wider parameter space to confirm if the propped area decreases with increase in cluster spacing. Figure 16 shows the propped area in Layer D as a function of cluster spacing varying from 20-100 ft., which corresponds to varying stage length from 100 ft. to 500 ft. There is a clear trend of decreasing propped area in the primary target layer with increase in cluster spacing with a reduction of about 40% from the 20 ft. case to the 100 ft. case. A similar reduction in observed in the combined propped area of formation D, E and F as well.
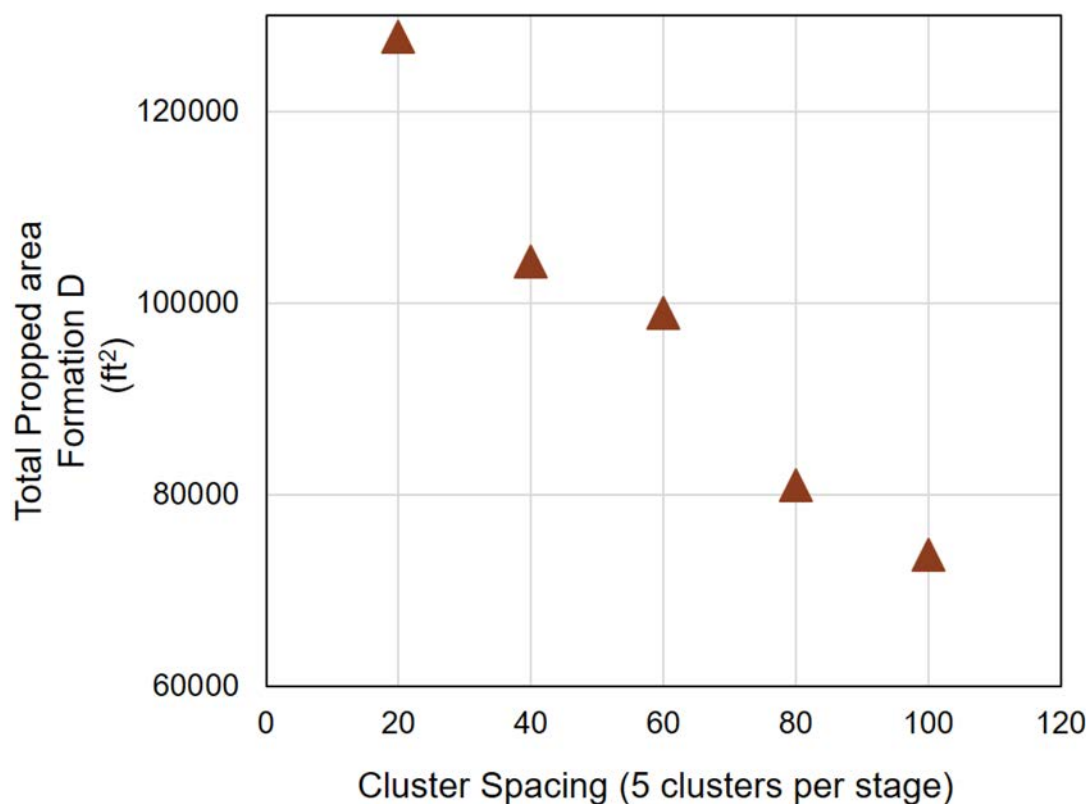

Figure 16—Variation of propped area in target formation as function of cluster spacing over a wider parameter space is shown for ACS-2. The propped area decreases with increase in cluster spacing as the stress shadow reduces and the individual fracture footprint approaches the single fracture case.

Three perforation cluster stage design: Propped area distribution for ACS-1

While for ACS-2, increasing stress shadow causes a more optimal stimulation, the interaction between stress shadow and the stress layering is very complex and needs to be analyzed carefully for individual cases. Figure 17 shows the distribution of the fracture and propped area for ACS-1. The decrease in cluster spacing from 200 ft. to 50 ft. shows a significant increase in both the fracture and propped area in layers D, E and F. However, decreasing the cluster spacing further causes more proppant placement and fracture area in layer C, resulting in the poor stimulation of the target zones. The difference in the stimulation of ACS-1 and ACS-2 is due to a variation in relative thickness of the target layer and the low stress layers. In case of ACS-1 the increased stress shadow is accommodated by wider lateral propagation of the fractures in the low stress layers, while in ACS-2 the thicker target layer D accommodates the fracture growth due to stress shadow.
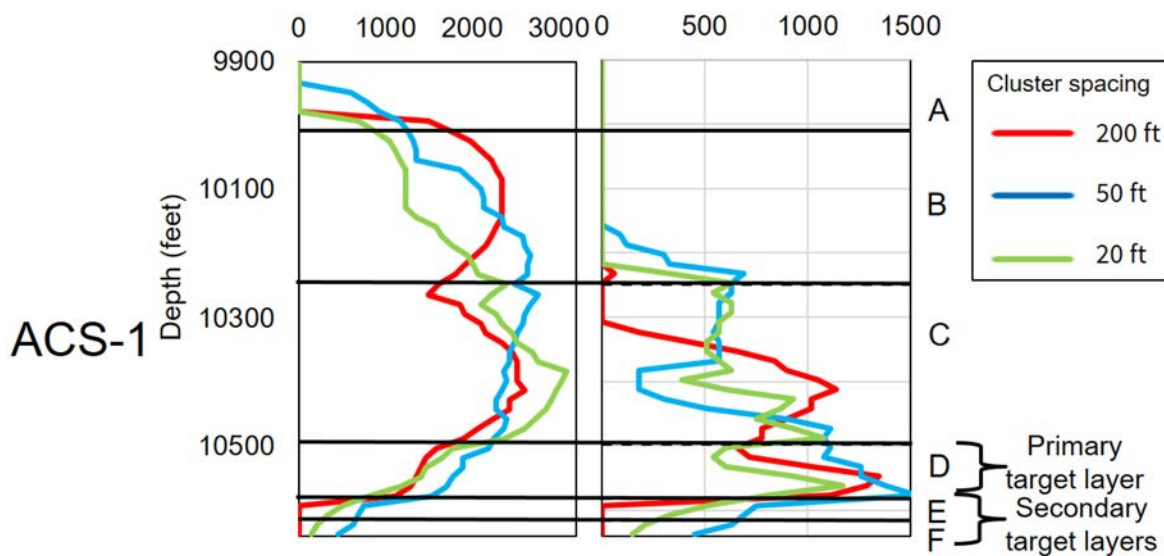
Figure 17—The distribution of total fracture area and propped area with depth for wells
ACS-1 and H-1 is shown for the 200 ft., 50 ft. and 20 ft. cluster spacing realizations.

The total fracture area and propped area for the three wells in target layers for all the cases is shown in Table 3

Table 3—Fracture and propped area for all the wells as a function of cluster spacing.

Stress profile	Cluster Spacing	Fracture area ft^2			Propped area ft^2		
		Total	Formation D/ Pay	D+E+F	Total	Formation D/ Pay	D+E+F
ACS-1	200	1.22E+06	1.23E+05	1.23E+05	5.65E+03	3.31E+03	3.31E+03
	50	1.38E+06	1.65E+05	2.03E+05	7.45E+03	4.08E+03	4.73E+03
	20	1.16E+06	1.24E+05	1.42E+05	5.67E+03	2.51E+03	2.85E+03
ACS-2	200	1.24E+06	5.58E+04	5.58E+04	5.01E+03	2.06E+03	2.06E+03
	50	1.08E+06	4.32E+04	2.12E+05	4.44E+03	1.54E+03	2.39E+03
	20	1.28E+06	2.07E+05	2.32E+05	7.05E+03	4.79E+03	5.27E+03
H-1	200	8.03E+05	6.19E+05	N.A.	6.40E+03	5.49E+03	N.A.
	50	9.72E+05	5.04E+05	N.A.	6.05E+03	4.97E+03	N.A.
	20	9.83E+05	5.36E+05	N.A.	6.60E+03	4.88E+03	N.A.